

Quantum Theory of Exciton Magnetic Moment: Interaction and Topological Effects

Authors: Gurjyot Sethi^{1,2}, Jiawei Ruan^{1,2}, Fang Zhang^{1,2}, Weichen Tang^{1,2}, Chen Hu^{1,2}, Mit Naik^{1,2}, and Steven G. Louie^{1,2*}

Affiliations:

¹Department of Physics, University of California at Berkeley, Berkeley, CA, USA.

²Materials Sciences Division, Lawrence Berkeley National Laboratory, Berkeley, CA, USA.

*Corresponding author: sglouie@berkeley.edu (S.G.L.)

Abstract: Combining magnetometry with optical spectroscopy has uncovered novel quantum phenomena and is emerging as a platform for quantum information science. Yet, the theory of magnetic response of excitons, correlated electron-hole pairs in semiconductors, remains incomplete due to insufficient treatment of electron-hole interaction and topological effects. In biased bilayer graphene, for instance, theoretical predictions of valley g-factor for p -excitons deviate from experiment by nearly an order of magnitude. Here, we develop a quantum theory of exciton orbital magnetic moment that reveals several conceptually new terms absent in prior theories, including an unforeseen contribution from exciton band quantum geometry. Our ab initio calculations yield results in excellent agreement with measurements, establishing the importance of a full theory including interaction and topological effects for the magnetic response of excitons.

Main Text: Using light to probe quantum materials has been at the forefront of discovering novel quantum phenomena, while also serving as a powerful diagnostic of material properties. Traditionally, optical spectroscopy has revealed energy gaps (1), excitonic resonances (2), and collective excitations (3). More recently, the combination of optics with magnetometry has emerged as a rich spectroscopic probe, capable of unveiling subtler aspects of correlated and topological matter. In particular, the magnetic response of optical excitations in materials provides a unique window into intrinsic magnetic orders (4), enables quantum control of magnetic properties through optical means (5, 6), and connects light-matter interactions to underlying quantum geometry (7, 8). Importantly, these capabilities extend beyond spectroscopy: magneto-optical platforms are now being actively explored for quantum information science, where light-matter excitations and spin degrees of freedom can function as optically addressable qubits (9), magnetic field-controlled quantum switches (10), and building blocks for quantum sensing technologies (11).

Central to many of these phenomena is the response of excitons, correlated electron-hole pairs, to external magnetic fields. Excitons dominate the optical response of semiconductors, especially in low dimensions (12), and mediate interactions between light, charge, and spin degrees of freedom. Two-dimensional (2D) semiconductors that possess three-fold rotational symmetry and broken inversion symmetry provide an especially fertile platform to access this interplay, since their valley degrees of freedom couple directly to external magnetic fields (7, 13). In such systems, exemplified by monolayer transition metal dichalcogenides (TMDs) and gapped multi-layer graphene, the conduction and valence bands in opposite valleys respond asymmetrically to the field, a consequence of non-zero berry curvature induced by inversion symmetry breaking (14). Excitons formed in these valleys therefore acquire opposite magnetic moments, giving rise to measurable Zeeman splitting of excitonic resonances in optical spectra. This valley-selective magnetic response provides a means to tune valley coherence (15), opening avenues for efficient valleytronic devices. Recent magneto-optical experiments in monolayer TMDs (16-19) and biased bilayer graphene (20) have demonstrated the valley Zeeman response of exciton peaks, quantified through an effective exciton valley g-factor.

Despite extensive experimental interest and its fundamental importance, a rigorous many-body quantum mechanical theory of the first-order response of exciton levels to an external magnetic field remains incomplete. To first-order in the magnetic field, the energy shift of exciton is proportional to its magnetic moment, including both spin and orbital contributions. Commonly employed theoretical approximations heuristically treat the exciton orbital magnetic moment as the difference between the electron (conduction) and hole (valence) bands' single-particle magnetic moments (21-23), neglecting critical e-h interactions and differences in exciton orbital character, as well as exciton band structure effects. More recent attempts have incorporated interactions by weighting the single-particle magnetic moment differences with the absolute value square of the \mathbf{k} -space exciton envelope function amplitude in the Brillouin zone (BZ) (24). Although intuitive, this approach falls short since it neglects the internal and center-of-mass (COM) dynamics of the excitons, particularly in systems like biased bilayer graphene (BBG) where the nontrivial band topology plays a significant role in the excitonic physics. Consequently, these approaches dramatically fail to explain the experimentally measured g-factors (20).

The fundamental issue in the theory of orbital magnetic moment for extended quasiparticle states (e.g., electronic or excitonic states that are Bloch waves in a crystal) lies in the correct quantum mechanical treatment of the orbital magnetic moment (or equivalently, position) operator (25-27). This complication, arising from the unbounded nature of the position operator, makes it nontrivial to evaluate the orbital contribution to the magnetic moment in a periodic solid. Previous approximate treatments of this issue result in important missing terms related to the internal exciton dynamics and the quantum geometry of the exciton band structure. Specifically, even at the single-particle level, the position operator matrix element in Bloch basis contains off-diagonal terms proportional to derivatives of delta functions in momentum space $\nabla_{\mathbf{k}}\delta(\mathbf{k} - \mathbf{k}')$, reflecting inherent nonlocalities in Bloch states. A very recent approach to calculate exciton valley g-factors considered off-diagonal matrix elements of the orbital moment operator in the band-state Bloch basis (28), but it still neglected this fundamental divergence, leading to an incomplete theory. Omitting these terms compromises gauge invariance and the physical consistency of the theory. This challenge is compounded critically in the case of excitons, which are composite objects formed from the material's constituent electron and hole Bloch states, and the excitons themselves are Bloch wavefunctions in their COM coordinates, leading to important physical consequences in the measured exciton orbital magnetic moment as manifested in the case of BBG.

In this work, we derive a full quantum mechanical expression for the exciton orbital magnetic moment within the many-body GW plus Bethe-Salpeter equation (GW-BSE) approach (29, 30), explicitly addressing the previously neglected divergent behavior of the magnetic moment operator in the Bloch basis. We introduce a periodic, wavelength-dependent magnetic field (which will be taken in the infinite wavelength limit later) as the applied external field since it leads to a mathematically well-behaved expression containing the position operator, enabling proper evaluation of its matrix elements. This procedure reveals new quantum corrections to the exciton magnetic moment beyond the conventional approximations. To avoid other divergence issue related to the COM motion of excitons, we further construct a localized exciton wave packet in its COM coordinates and subsequently delocalize it back to an exciton Bloch state. A schematic of our approach for the derivation the exciton magnetic moment is shown in Fig. 1a. This theoretical procedure provides a well-grounded conceptual framework for our derivation and yields a final gauge-invariant expression for the exciton magnetic moment, which naturally decomposes into three physically distinct contributions (Fig. 1b): the difference between the single-particle Berry-phase-corrected orbital moments of the excited electron and hole, the envelope function phase winding contribution associated with relative e-h motion, and the e-h COM contribution arising from exciton band quantum geometry effects. Applying our derived expression to biased bilayer graphene employing ab initio GW-BSE (29, 30) results, we compute the exciton g-factors for the *s*- and *p*-type excitons, obtaining excellent agreement with experimental data and clearly identifying the importance of the newly discovered quantum contributions as detailed below.

Quantum theory of exciton magnetic moment with the ab initio GW-BSE approach

To determine the orbital magnetic moment of an exciton state with quantum number n and COM momentum \mathbf{Q} , $\mu_{n\mathbf{Q}}^X$, we consider its first-order change in energy $\delta E_{n\mathbf{Q}}^X$ in the presence of an uniform magnetic field \mathbf{B} and relate it to $\delta E_{n\mathbf{Q}}^X = -\mu_{n\mathbf{Q}}^X \cdot \mathbf{B}$ (see supplementary text, section 1). First, we consider the unperturbed exciton Hamiltonian, H^X , for the excited electron and hole within any effective 2-particle formulation, example, the ab initio GW-BSE approach. Because of the translation symmetry of the crystal, the COM wavevector of the excitonic states is a good quantum number, leading to $H^X = \sum_{\mathbf{Q}} H^X(\mathbf{Q})$. For each \mathbf{Q} , the exciton Hamiltonian matrix elements within the standard GW-BSE approach (30) expressed in the free e-h band state basis, $|v\mathbf{c}\mathbf{k}\mathbf{Q}\rangle = |c\mathbf{k} + \frac{\mathbf{Q}}{2}\rangle \otimes |v\mathbf{k} - \frac{\mathbf{Q}}{2}\rangle$, are:

$$H_{v\mathbf{c}\mathbf{k}, v'\mathbf{c}'\mathbf{k}'}^X(\mathbf{Q}) = \langle v\mathbf{c}\mathbf{k}\mathbf{Q} | H^X | v'\mathbf{c}'\mathbf{k}'\mathbf{Q} \rangle = (\epsilon_{c\mathbf{k}+\mathbf{Q}/2} - \epsilon_{v\mathbf{k}-\mathbf{Q}/2}) \delta_{vv'} \delta_{cc'} \delta_{\mathbf{k}\mathbf{k}'} + K_{v\mathbf{c}\mathbf{k}, v'\mathbf{c}'\mathbf{k}'}^{eh}(\mathbf{Q}), \quad (1)$$

where K^{eh} is the e-h interaction kernel. Diagonalization of the Hamiltonian in Eq. 1 yields the n th exciton with energies $E_{n\mathbf{Q}}^X$ and eigenvectors $A_{v\mathbf{c}\mathbf{k}}^{n\mathbf{Q}}$ (called the exciton envelope functions in \mathbf{k} -space). The corresponding exciton state vector is given as:

$$|X_{n\mathbf{Q}}\rangle = \sum_{v\mathbf{c}\mathbf{k}} A_{v\mathbf{c}\mathbf{k}}^{n\mathbf{Q}} |v\mathbf{c}\mathbf{k}\mathbf{Q}\rangle = e^{i\mathbf{Q} \cdot (\frac{\mathbf{r}_e + \mathbf{r}_h}{2})} \sum_{v\mathbf{c}\mathbf{k}} A_{v\mathbf{c}\mathbf{k}}^{n\mathbf{Q}} e^{i\mathbf{k} \cdot (\mathbf{r}_e - \mathbf{r}_h)} |u_{c\mathbf{k}+\mathbf{Q}/2}\rangle \otimes |u_{v\mathbf{k}-\mathbf{Q}/2}\rangle = e^{i\mathbf{Q} \cdot \mathbf{R}} |u_{n\mathbf{Q}}^X\rangle \quad (2)$$

where $|u_{n\mathbf{Q}}^X\rangle$ defined through Eq. 2 is the periodic part of the n th exciton Bloch wavefunction. The change in exciton energy under the \mathbf{B} field perturbation can be determined by evaluating the matrix elements of the perturbed excitonic Hamiltonian \tilde{H}^X in the *unperturbed* excitonic basis $|X_{n\mathbf{Q}}\rangle$, i.e., by evaluating $\langle X_{n\mathbf{Q}} | \tilde{H}^X | X_{n'\mathbf{Q}'} \rangle$. Assuming the e-h interaction remains unperturbed by a weak field (i.e., $\tilde{K}^{eh} \approx K^{eh}$) which is expected to be valid in most experiment setups, it may be shown that, up to first order in the magnetic field, the perturbed Hamiltonian matrix elements (see supplementary text, section 2) are:

$$\begin{aligned} \langle X_{n\mathbf{Q}} | \tilde{H}^X | X_{n'\mathbf{Q}'} \rangle &= \delta_{\mathbf{Q}\mathbf{Q}'} \epsilon_{n\mathbf{Q}}^X - \\ \mathbf{B} \cdot \sum_{v\mathbf{c}\mathbf{k}} \left[\sum_{c'\mathbf{k}'} A_{v\mathbf{c}\mathbf{k}}^{n\mathbf{Q}*} A_{v'\mathbf{c}'\mathbf{k}'}^{n'\mathbf{Q}'} \delta_{\mathbf{k}-\frac{\mathbf{Q}}{2}, \mathbf{k}'-\frac{\mathbf{Q}'}{2}} \left\langle c\mathbf{k} + \frac{\mathbf{Q}}{2} \right| \hat{\mu} \left| c'\mathbf{k}' + \frac{\mathbf{Q}'}{2} \right\rangle - \sum_{v'\mathbf{k}'} A_{v\mathbf{c}\mathbf{k}}^{n\mathbf{Q}*} A_{v'\mathbf{c}'\mathbf{k}'}^{n'\mathbf{Q}'} \delta_{\mathbf{k}+\frac{\mathbf{Q}}{2}, \mathbf{k}'+\frac{\mathbf{Q}'}{2}} \left\langle v'\mathbf{k}' - \frac{\mathbf{Q}'}{2} \right| \hat{\mu} \left| v\mathbf{k} - \frac{\mathbf{Q}}{2} \right\rangle \right]. \end{aligned} \quad (3)$$

In the present work, for simplicity, we explicitly drop the spin Zeeman contribution to the magnetic moment, as spin-dependent terms vanish for the like-spin-transitions excitons (optically bright) considered here. But the spin contributions can be straightforwardly integrated into our formalism if required. Following Eq. 3, to accurately evaluate the orbital magnetic moment of excitons, we require matrix elements of the magnetic moment operator $\hat{\mu}$ in the Bloch band-state basis, which for a uniform magnetic field would be $\hat{\mu} = -\frac{e}{2} \hat{\mathbf{r}} \times \hat{\mathbf{v}}$. However, in this basis $\hat{\mathbf{r}}$ becomes very tricky to handle - specifically, it introduces divergences in Eq. 3 due to its off-diagonal terms in \mathbf{k} and \mathbf{k}' which involve the factor $\nabla_{\mathbf{k}} \delta(\mathbf{k} - \mathbf{k}')$ from intra-band contributions (25) (see supplementary text, section 3). Prior treatments of the exciton valley g-factor have basically ignored these subtle (but physically important) divergent terms by assuming the matrix elements to be diagonal in the momentum and/or the band index (21-24, 28). To address this subtlety, we introduce a periodic analog of the position operator characterized by a wavevector \mathbf{q} : $\hat{\mathbf{r}} \rightarrow \hat{\mathbf{r}}_{\mathbf{q}} = -i\nabla_{\mathbf{q}} e^{i\mathbf{q} \cdot \hat{\mathbf{r}}}$, which is well-behaved in the Bloch basis and smoothly recovers to the original position operator in the long-wavelength limit ($\mathbf{q} \rightarrow 0$). Accordingly, we replace the orbital magnetic moment operator as: $\hat{\mu}_{\mathbf{q}} = \frac{e}{2} i\nabla_{\mathbf{q}} (e^{i\mathbf{q} \cdot \hat{\mathbf{r}}}) \times \hat{\mathbf{v}} = \frac{e}{2} i\nabla_{\mathbf{q}} \times e^{i\mathbf{q} \cdot \hat{\mathbf{r}}} \hat{\mathbf{v}}$ in

the evaluation of Eq. 3 and then take the $\mathbf{q} = 0$ limit. Physically, this transformation can be viewed as evaluating exciton energy shifts under a spatially periodic magnetic field (31, 32) characterized by wavevector \mathbf{q} and then subsequently taking the long-wavelength limit to recover the uniform magnetic field scenario. Following this procedure one obtains the expression:

$$\begin{aligned}
\langle X_{n\mathbf{Q}} | \tilde{H}^X | X_{n'\mathbf{Q}'} \rangle = & \delta_{\mathbf{Q}\mathbf{Q}'} E_{n\mathbf{Q}}^X - \delta_{\mathbf{Q}\mathbf{Q}'} \mathbf{B} \cdot \sum_{v\mathbf{c}\mathbf{k}} \left\{ \sum_{c'} A_{v\mathbf{c}\mathbf{k}}^{n\mathbf{Q}*} A_{v\mathbf{c}'\mathbf{k}}^{n'\mathbf{Q}} \boldsymbol{\mu}_{cc'\mathbf{k}+\frac{\mathbf{Q}}{2}} - \sum_{v'} A_{v\mathbf{c}\mathbf{k}}^{n\mathbf{Q}*} A_{v'\mathbf{c}\mathbf{k}}^{n'\mathbf{Q}} \boldsymbol{\mu}'_{v'v\mathbf{k}-\frac{\mathbf{Q}}{2}} \right\} \\
& - \frac{e}{2\hbar} \delta_{\mathbf{Q}\mathbf{Q}'} \mathbf{B} \cdot \sum_{v\mathbf{c}\mathbf{k}} \left\{ \sum_{c'} A_{v\mathbf{c}\mathbf{k}}^{n\mathbf{Q}*} A_{v\mathbf{c}'\mathbf{k}}^{n'\mathbf{Q}} \left(\nabla_{\mathbf{k}} \epsilon_{c\mathbf{k}} \Big|_{\mathbf{k}+\frac{\mathbf{Q}}{2}} \times \mathcal{A}_{cc'\mathbf{k}+\frac{\mathbf{Q}}{2}} \right) - \sum_{v'} A_{v\mathbf{c}\mathbf{k}}^{n\mathbf{Q}*} A_{v'\mathbf{c}\mathbf{k}}^{n'\mathbf{Q}} \left(\nabla_{\mathbf{k}} \epsilon_{v\mathbf{k}} \Big|_{\mathbf{k}-\frac{\mathbf{Q}}{2}} \times \mathcal{A}_{v'v\mathbf{k}-\frac{\mathbf{Q}}{2}} \right) \right\} \\
& - \frac{e}{4i} \delta_{\mathbf{Q}\mathbf{Q}'} \mathbf{B} \cdot \sum_{v\mathbf{c}\mathbf{k}} \left\{ \sum_{c'} \left(A_{v\mathbf{c}\mathbf{k}}^{n\mathbf{Q}*} \nabla_{\mathbf{k}} A_{v\mathbf{c}'\mathbf{k}}^{n'\mathbf{Q}} \times \mathbf{v}_{cc'\mathbf{k}+\frac{\mathbf{Q}}{2}} \right) + \sum_{v'} \left(A_{v\mathbf{c}\mathbf{k}}^{n\mathbf{Q}*} \nabla_{\mathbf{k}} A_{v'\mathbf{c}\mathbf{k}}^{n'\mathbf{Q}} \times \mathbf{v}_{v'v\mathbf{k}-\frac{\mathbf{Q}}{2}} \right) \right\} \\
& - \frac{e}{2i} \delta_{\mathbf{Q}\mathbf{Q}'} \mathbf{B} \cdot \sum_{v\mathbf{c}\mathbf{k}} \left\{ \sum_{c'} \left(A_{v\mathbf{c}\mathbf{k}}^{n\mathbf{Q}*} \nabla_{\mathbf{Q}} A_{v\mathbf{c}'\mathbf{k}}^{n'\mathbf{Q}} \times \mathbf{v}_{cc'\mathbf{k}+\frac{\mathbf{Q}}{2}} \right) - \sum_{v'} \left(A_{v\mathbf{c}\mathbf{k}}^{n\mathbf{Q}*} \nabla_{\mathbf{Q}} A_{v'\mathbf{c}\mathbf{k}}^{n'\mathbf{Q}} \times \mathbf{v}_{v'v\mathbf{k}-\frac{\mathbf{Q}}{2}} \right) \right\} \\
& - \frac{e}{2i} \mathbf{B} \cdot \left((\nabla_{\mathbf{Q}} \delta_{\mathbf{Q}\mathbf{Q}'}) \times \sum_{v\mathbf{c}\mathbf{k}} \left\{ \sum_{c'} A_{v\mathbf{c}\mathbf{k}}^{n\mathbf{Q}*} A_{v\mathbf{c}'\mathbf{k}}^{n'\mathbf{Q}} \mathbf{v}_{cc'\mathbf{k}+\frac{\mathbf{Q}}{2}} - \sum_{v'} A_{v\mathbf{c}\mathbf{k}}^{n\mathbf{Q}*} A_{v'\mathbf{c}\mathbf{k}}^{n'\mathbf{Q}} \mathbf{v}_{v'v\mathbf{k}-\frac{\mathbf{Q}}{2}} \right\} \right), \tag{4}
\end{aligned}$$

where the notations used are defined as follows: We generalize the notion of a single-particle magnetic moment to the multi-band case by defining two matrices: $\boldsymbol{\mu}_{ij\mathbf{k}} = \frac{e}{2i\hbar} \langle \nabla_{\mathbf{k}} u_{i\mathbf{k}} | \times [H_{\mathbf{k}} - \epsilon_{i\mathbf{k}}] | \nabla_{\mathbf{k}} u_{j\mathbf{k}} \rangle$, and $\boldsymbol{\mu}'_{ij\mathbf{k}} = \frac{e}{2i\hbar} \langle \nabla_{\mathbf{k}} u_{i\mathbf{k}} | \times [H_{\mathbf{k}} - \epsilon_{j\mathbf{k}}] | \nabla_{\mathbf{k}} u_{j\mathbf{k}} \rangle$ with $H_{\mathbf{k}} = e^{-i\mathbf{k}\cdot\mathbf{r}} H e^{i\mathbf{k}\cdot\mathbf{r}}$. Note that the two matrices $\boldsymbol{\mu}_{ij\mathbf{k}}$, and $\boldsymbol{\mu}'_{ij\mathbf{k}}$ come from the placement of $\epsilon_{i\mathbf{k}}$ or $\epsilon_{j\mathbf{k}}$ that goes inside the expression, respectively. The single-particle inter-band Berry connection is given by: $\mathcal{A}_{ij\mathbf{k}} = i \langle u_{i\mathbf{k}} | \nabla_{\mathbf{k}} u_{j\mathbf{k}} \rangle$, and the velocity matrix by: $\mathbf{v}_{ij\mathbf{k}} = \langle u_{i\mathbf{k}} | \hat{\mathbf{v}}(\mathbf{k}) | u_{j\mathbf{k}} \rangle = \frac{1}{\hbar} (\epsilon_{j\mathbf{k}} - \epsilon_{i\mathbf{k}}) \langle u_{i\mathbf{k}} | \nabla_{\mathbf{k}} u_{j\mathbf{k}} \rangle + \frac{1}{\hbar} \delta_{ij} \nabla_{\mathbf{k}} \epsilon_{i\mathbf{k}}$.

From our theory, there are now five terms on the right-hand-side (RHS) of Eq. 4 that are linear in \mathbf{B} . All five terms contribute to the final value for the exciton orbital magnetic moment. The first term may be viewed as corresponding to a multi-band version of the conventional expression used in the literature (24, 28), while the remaining four terms are new and represent novel contributions arising from the rigorous treatment of the previously neglected divergences associated with the $\hat{\mathbf{r}}$ operator. Importantly, the final two terms in Eq. 4 explicitly involve derivatives of quantities with respect to \mathbf{Q} , highlighting the critical role of the exciton COM motions in a complete description of the exciton magnetic moment. In particular, the last term contains the quantity $\nabla_{\mathbf{Q}} \delta_{\mathbf{Q}\mathbf{Q}'}$ which appears singular and requires careful treatment. This quantity closely resembles the singularity arising from the $\hat{\mathbf{r}}$ operator in the single-particle Bloch-state representation. However, in this excitonic context, the singular behavior here originates from the fact that we consider the energy change induced by the \mathbf{B} field of an extended exciton with a COM Bloch wavefunction of a specific \mathbf{Q} . A more physical approach would be to consider an exciton wave-packet of finite width, compute its change in energy, and subsequently take the wave-packet width to the infinite limit, which requires additional formulation to yield physically meaningful result.

To address the last term in Eq. 4 rigorously, we first construct a localized exciton wave-packet (33, 34) centered at $\mathbf{R}_{\mathbf{c}}$ in real-space COM coordinates formed by a superposition of exciton Bloch wavefunctions, $|W_{n\mathbf{Q}_{\mathbf{c}}}\rangle = \sum_{\mathbf{Q}} w(\mathbf{Q} - \mathbf{Q}_{\mathbf{c}}) |X_{n\mathbf{Q}}\rangle$, where the function $w(\mathbf{Q} - \mathbf{Q}_{\mathbf{c}})$ is localized and peaked around $\mathbf{Q}_{\mathbf{c}}$ in COM momentum space satisfying $\sum_{\mathbf{Q}} \mathbf{Q} |w(\mathbf{Q} - \mathbf{Q}_{\mathbf{c}})|^2 = \mathbf{Q}_{\mathbf{c}}$. As a consequence, this exciton wave-packet is centered at

$$\langle W_{n\mathbf{Q}_c} | \mathbf{R} | W_{n\mathbf{Q}_c} \rangle = \mathbf{R}_c = i \sum_{\mathbf{Q}} w^*(\mathbf{Q} - \mathbf{Q}_c) \nabla_{\mathbf{Q}} w(\mathbf{Q} - \mathbf{Q}_c) + \sum_{\mathbf{Q}} |w(\mathbf{Q} - \mathbf{Q}_c)|^2 \mathcal{A}_{n\mathbf{Q}}^X. \quad (5)$$

Here, $\mathcal{A}_{n\mathbf{Q}}^X$ is the *exciton band* Berry connection: $\mathcal{A}_{n\mathbf{Q}}^X = i \langle u_{n\mathbf{Q}}^X | \nabla_{\mathbf{Q}} u_{n\mathbf{Q}}^X \rangle$. Owing to the localized nature of $|W_{n\mathbf{Q}_c}\rangle$ in the real-space COM coordinates, matrix element of the perturbed exciton Hamiltonian in the wave-packet basis is well-defined. We evaluate $\langle W_{n\mathbf{Q}_c} | \tilde{H}^X | W_{n\mathbf{Q}_c} \rangle$ (see supplementary text, section 4), and take the limit $|w(\mathbf{Q} - \mathbf{Q}_c)|^2 \rightarrow \delta(\mathbf{Q} - \mathbf{Q}_c)$, i.e., we delocalize the wave-packet back to an exciton Bloch wavefunction with COM momentum \mathbf{Q}_c . We finally obtain our main result - a gauge invariant general expression for the exciton orbital magnetic moment of the n th exciton - as follows (see supplementary text, section 5):

$$\begin{aligned} \mu_{n\mathbf{Q}}^X = & \sum_{vck} \left\{ \sum_{c'} A_{vck}^{nQ*} A_{vc'k}^{nQ} \mu_{cc'k+\frac{\mathbf{Q}}{2}} - \sum_{v'} A_{vck}^{nQ*} A_{v'ck}^{nQ} \mu_{v'vk-\frac{\mathbf{Q}}{2}} \right\} \\ & + \frac{e}{2\hbar} \sum_{vck} \left\{ \sum_{c'} A_{vck}^{nQ*} A_{vc'k}^{nQ} \left(\nabla_{\mathbf{k}} \epsilon_{ck} \Big|_{\mathbf{k}+\frac{\mathbf{Q}}{2}} \times \mathcal{A}_{cc'k+\frac{\mathbf{Q}}{2}} \right) - \sum_{v'} A_{vck}^{nQ*} A_{v'ck}^{nQ} \left(\nabla_{\mathbf{k}} \epsilon_{vk} \Big|_{\mathbf{k}-\frac{\mathbf{Q}}{2}} \times \mathcal{A}_{v'vk-\frac{\mathbf{Q}}{2}} \right) \right\} \\ & + \frac{e}{4i} \sum_{vck} \left\{ \sum_{c'} \left(A_{vck}^{nQ*} \nabla_{\mathbf{k}} A_{vc'k}^{nQ} \times \mathbf{v}_{cc'k+\frac{\mathbf{Q}}{2}} \right) + \sum_{v'} \left(A_{vck}^{nQ*} \nabla_{\mathbf{k}} A_{v'ck}^{nQ} \times \mathbf{v}_{v'vk-\frac{\mathbf{Q}}{2}} \right) \right\} \\ & + \frac{e}{2\mathbb{I}\mathbb{I}} \sum_{vck} \left\{ \sum_{c'} \left(A_{vck}^{nQ*} \nabla_{\mathbf{Q}} A_{vc'k}^{nQ} \times \mathbf{v}_{cc'k+\frac{\mathbf{Q}}{2}} \right) - \sum_{v'} \left(A_{vck}^{nQ*} \nabla_{\mathbf{Q}} A_{v'ck}^{nQ} \times \mathbf{v}_{v'vk-\frac{\mathbf{Q}}{2}} \right) \right\} \\ & + \frac{e}{2} \left(\mathcal{A}_{n\mathbf{Q}}^X \times \sum_{vck} \left\{ \sum_{c'} A_{vck}^{nQ*} A_{vc'k}^{nQ} \mathbf{v}_{cc'k+\frac{\mathbf{Q}}{2}} - \sum_{v'} A_{vck}^{nQ*} A_{v'ck}^{nQ} \mathbf{v}_{v'vk-\frac{\mathbf{Q}}{2}} \right\} \right), \end{aligned} \quad (6)$$

Physically, we shall express the exciton orbital magnetic moment by regrouping the above five terms into three groups with named labels (whose distinct physical meaning will become clear in the two-band limit discussion below):

$$\mu_{n\mathbf{Q}}^X = \mu_{n\mathbf{Q}}^{X,sp} + \mu_{n\mathbf{Q}}^{X,rel} + \mu_{n\mathbf{Q}}^{X,COM}, \quad (7)$$

where, in terms of the RHS of Eq. 6, $\mu_{n\mathbf{Q}}^{X,sp}$ is the sum of terms #1 and #2 where “*sp*” stands for “single-particle”, $\mu_{n\mathbf{Q}}^{X,rel}$ is term #3 where “*rel*” stands for “relative”, and $\mu_{n\mathbf{Q}}^{X,COM}$ is the sum of terms #4 and #5 where “*COM*” stands for “center-of-mass”.

Two-band limit of general theory

To gain physical insight into the different contributions to the general expression for the exciton orbital moment given by Eq. 6, which is the central result of this study, we consider the simple 2-band case where the exciton state is composed of free e-h pairs involving a single valence (v) and a single conduction band (c). In this limit, the three labeled terms for the exciton orbital magnetic moment $\mu_{n\mathbf{Q}}^X$ on the RHS of Eq. 7 simplify and yield the following physical pictures.

The e and h single-particle moments contribution ($\mu_{n\mathbf{Q}}^{X,sp}$): This contribution originates from the single-particle orbital magnetic moments of the conduction and valence band states that compose the exciton, and corresponds to the first two terms on the RHS of Eq. 6 which reduce to:

$$\begin{aligned} \mu_{n\mathbf{Q}}^{X,sp}(2band) &= \sum_{\mathbf{k}} |A_{\mathbf{k}}^{n\mathbf{Q}}|^2 \left(\mu_{c\mathbf{k}+\frac{\mathbf{Q}}{2}} - \mu_{v\mathbf{k}-\frac{\mathbf{Q}}{2}} \right) \\ &+ \frac{e}{2\hbar} \sum_{\mathbf{k}} |A_{\mathbf{k}}^{n\mathbf{Q}}|^2 \left(\nabla_{\mathbf{k}} \epsilon_{c\mathbf{k}}|_{\mathbf{k}+\frac{\mathbf{Q}}{2}} \times \mathcal{A}_{c\mathbf{k}+\frac{\mathbf{Q}}{2}} - \nabla_{\mathbf{k}} \epsilon_{v\mathbf{k}}|_{\mathbf{k}-\frac{\mathbf{Q}}{2}} \times \mathcal{A}_{v\mathbf{k}-\frac{\mathbf{Q}}{2}} \right). \end{aligned} \quad (8)$$

Specifically, this contribution comes from the single-particle band structure. It corresponds to the difference between the free electron and hole orbital magnetic moments, averaged over the momentum space (\mathbf{k} -space) using the exciton envelope function amplitude square which is the 2-band limit of the first term in the RHS of Eq. 6 (as has been used in the literature so far (24)), but with an important quantum correction. This correction (given by the second term on RHS in Eq. 6) emerges naturally from our rigorous treatment of the orbital magnetic moment operator. Semi-classically, it can be interpreted as a Berry-phase modification of the density of states (35). In the presence of a magnetic field, Berry curvature introduces an anomalous term into the electron group velocity, consequently altering the density of states and modifying integrals involving single-particle quantities over the BZ (36). As the first term on the RHS of Eq. 8 involves such integrals, the Berry-phase correction manifests explicitly in our formalism through the second term which to our knowledge is neglected in previous studies even at this single-particle level.

The e-h relative motion contribution ($\mu_{n\mathbf{Q}}^{X,rel}$): The second contribution, given by:

$$\mu_{s\mathbf{Q}}^{X,rel}(2band) = \frac{e}{4i\hbar} \sum_{\mathbf{k}} A_{\mathbf{k}}^{n\mathbf{Q}*} \nabla_{\mathbf{k}} A_{\mathbf{k}}^{n\mathbf{Q}} \times \left(\nabla_{\mathbf{k}} \epsilon_{c\mathbf{k}}|_{\mathbf{k}+\frac{\mathbf{Q}}{2}} + \nabla_{\mathbf{k}} \epsilon_{v\mathbf{k}}|_{\mathbf{k}-\frac{\mathbf{Q}}{2}} \right), \quad (9)$$

arises from the relative motion of the electron and hole constituting the exciton. This corresponds to the 3rd term on the RHS of Eq. 6 in the 2-band limit. In relative coordinates, the exciton's internal structure is captured by the magnitude and phase of its envelope function. Specifically, the term $A_{\mathbf{k}}^{n\mathbf{Q}*} \nabla_{\mathbf{k}} A_{\mathbf{k}}^{n\mathbf{Q}}$ characterizes the phase winding of the exciton envelope function in the BZ. This winding couples directly to the relative e-h velocity, given by half of the difference between the electron and hole group velocities. Note that in Eq. 9, the quantities related to velocities are given in term of the \mathbf{k} -derivatives of the energy of electron bands; hence, the hole velocity corresponds to the negative of the electron valence-band group velocity. The nature of the envelope-function winding, distinguishing the character (e.g., between s-like and p-like symmetries) of the exciton, which is determined by its phase structure, introduces a pseudospin degree of freedom (37) that contributes to the orbital magnetic moment of the exciton.

The e-h COM motion contribution ($\mu_{n\mathbf{Q}}^{X,COM}$): The third contribution to $\mu_{n\mathbf{Q}}^X$ arises from the COM motion of the exciton. In the 2-band limit, it is given by:

$$\begin{aligned} \mu_{n\mathbf{Q}}^{X,COM}(2band) &= \frac{e}{2i\hbar} \sum_{\mathbf{k}} (A_{\mathbf{k}}^{n\mathbf{Q}*} \nabla_{\mathbf{Q}} A_{\mathbf{k}}^{n\mathbf{Q}}) \times \left(\nabla_{\mathbf{k}} \epsilon_{c\mathbf{k}}|_{\mathbf{k}+\frac{\mathbf{Q}}{2}} - \nabla_{\mathbf{k}} \epsilon_{v\mathbf{k}}|_{\mathbf{k}-\frac{\mathbf{Q}}{2}} \right) \\ &+ \frac{e}{2\hbar} (\mathcal{A}_{n\mathbf{Q}}^X) \times \sum_{\mathbf{k}} |A_{\mathbf{k}}^{n\mathbf{Q}}|^2 \left(\nabla_{\mathbf{k}} \epsilon_{c\mathbf{k}}|_{\mathbf{k}+\frac{\mathbf{Q}}{2}} - \nabla_{\mathbf{k}} \epsilon_{v\mathbf{k}}|_{\mathbf{k}-\frac{\mathbf{Q}}{2}} \right). \end{aligned} \quad (10)$$

This contribution reduces from the 4th and 5th terms on the RHS of Eq. 6. While a naïve classical perspective might suggest that the COM dynamics of a neutral exciton should not couple to a magnetic field, our quantum mechanical derivation reveals two new effects related to the quantum geometry of the exciton band structure: (a) an effect originating from the phase winding of the exciton wavefunction in \mathbf{Q} -space, and (b) an effect from the exciton band Berry connection. Effect *a* is captured by the term containing $A_{\mathbf{k}}^{n\mathbf{Q}*} \nabla_{\mathbf{Q}} A_{\mathbf{k}}^{n\mathbf{Q}}$, which describes how the phase of the exciton envelope function evolves with \mathbf{Q} and thus produces a pseudospin-like structure

associated with the exciton COM motion. This term appears as a cross product with the exciton's COM velocity, introducing a contribution to the orbital magnetic moment of the exciton. Effect *b* is a correction involving the exciton band Berry connection $\mathcal{A}_{n\mathbf{Q}}^X$, analogous to the single-particle case, where the Berry curvature modifies the group velocity of Bloch states (36). $\mathcal{A}_{n\mathbf{Q}}^X$ gives rise to anomalous excitonic COM motion in external fields (34) and consequently an orbital magnetic moment contribution.

Excitons in uniform magnetic field in biased bilayer graphene: theory vs experiment

We apply our full quantum expression (i.e., Eq. 6) for $\mu_{n\mathbf{Q}}^X$ to compute the exciton valley g-factor in a representative 2D material system – the biased bilayer graphene (BBG) – which has been experimentally measured (20). BBG consists of a Bernal-stacked (AB-stacked) graphene bilayer subjected to an external out-of-plane electric field (38-40). Experimental measurements on BBG are typically performed on samples encapsulated with hexagonal boron-nitride (hBN). In our study, we first perform ground-state density functional theory (DFT) calculations for BBG including the effect of hBN encapsulation (Fig. 2a). The quasiparticle band structure and excitonic properties are computed within the ab initio GW (29) and GW-BSE (30) approaches respectively (as detailed in methods). The quasiparticle band gap for the hBN encapsulated system with an out-of-plane field of 0.10 eV/Å is found to be 161 meV, significantly larger than the corresponding DFT-LDA Kohn-Sham gap of 72 meV, reflecting strong electron self-energy effects. The top valence and bottom conduction bands near the K and K' valleys exhibit a Mexican-hat-like dispersion (Fig. 2b), with no2 particle-hole asymmetry, leading to a non-zero difference in their single-particle orbital magnetic moments (Fig. 2c) (also see supplementary text, section 6).

The calculated optical absorption spectrum of BBG for normal incident linear polarized light is shown in Fig. 3a. Two pronounced excitonic resonances emerge below the quasiparticle gap, E_g , corresponding to the lowest-lying bound *s*- and *p*-type excitons with $\mathbf{Q} = 0$, respectively. We note that each peak consists of two degenerate exciton states from the two valleys K and K' due to time-reversal symmetry. Fig. 3b and Fig. 3c present the magnitude squared and phase of the exciton envelope functions in \mathbf{k} -space near the K point from the first peak and the second peak, respectively. Both exhibit clear threefold rotational symmetry around K. The exciton from the second peak (Fig. 3c) exhibits a 2π clockwise phase winding around K, corresponding to a winding number of +1, and a single nodal structure in its envelope function amplitude consistent with *p*-like symmetry. In contrast, the exciton from the lowest-energy peak (Fig. 3b) is node-less with no phase winding, indicative of an *s*-like state. An examination of the computed \mathbf{k} -dependent optical transition matrix elements between the valence and the conduction band for normal-incident circularly polarized light shows that, in the K (K') valley, it has a phase winding number of 0 (−1) or −1 (0), depending on the handedness of the light polarization. This behavior originating from the nontrivial pseudospin texture of the conduction and valence band states and explains why both *s* and *p*-like excitons are optically active, according to the Cao-Wu-Louie (CWL) winding-number optical selection rules for 2D excitons (37).

The exciton band dispersion near COM momentum $\mathbf{Q} = \Gamma$ is shown in Fig. 4a. At $\mathbf{Q} = \Gamma$, time-reversal symmetry ensures that the excitonic states are valley-degenerate, with the envelope functions localized around $\mathbf{k} = \text{K}$ and K' respectively. However, at finite \mathbf{Q} , the inter-valley e-h exchange interaction mixes the valley components (41). Notably, the *p*-exciton branches split with increasing $|\mathbf{Q}|$ yielding a lower parabolic branch and an upper branch exhibiting a characteristic v-shaped nonanalyticity, a behavior originating from the interplay between inter- and intra-valley exchange interactions. Such effects have also been reported in other 2D materials including monolayers of MoS₂ (41, 42), hBN (43), and black phosphorus (44). Importantly, this splitting is more prominent for the bright *p*-exciton, as the magnitude of the exchange scattering at small \mathbf{Q} scales with the oscillator strength (41), which is significantly smaller for the nearly dark *s*-excitons.

Furthermore, the excitonic bands carry a pseudospin texture inherited from their valley composition (41). In Fig. 4b, we plot the pseudospin texture of the p -exciton branches, confirming a phase winding number of ± 2 .

These rich excitonic properties make BBG a compelling platform for exploring the new additional contributions to the exciton magnetic moment predicted by our theory as given in Eq. 6, namely, those arising from single-particle and exciton band quantum geometry, envelope-function phase winding, and center-of-mass pseudospin. Moreover, BBG provides experimental access to these effects: recent photocurrent spectroscopy measurements reported the exciton valley g -factors (defined to be the absolute value of the difference in the exciton orbital moments from the two valleys divided by Bohr Magneton (μ_B)) of the lowest s - and p -excitons (20). At zero magnetic field, a single peak is observed, which splits into two under an applied out-of-plane magnetic field since the orbital magnetic moments of the two excitons, predominantly coming from the two different valleys, are different. The measured magnitude of these splitting, extracted via linear fitting, yields an exciton valley g -factor of $g_s = 19.8 \pm 0.1$, and $g_p = 1.4 \pm 0.8$, and is summarized in Table 1.

A common and most simplified approximation in the literature (21, 22) is to estimate the exciton orbital magnetic moment by evaluating the single-particle conduction-valence band moment difference (Fig. 2c) at the band edge, neglecting the exciton's momentum-space wavefunction as well as any band Berry-curvature effects. Noting that, for the bright (like-spin transitions) excitons the spin contribution is zero, this gives an effective valley g -factor of

$$g = \frac{1}{\mu_B} |[\mu_{c\mathbf{k}=\mathbf{K}} - \mu_{v\mathbf{k}=\mathbf{K}}]_z - [\mu_{c\mathbf{k}=\mathbf{K}'} - \mu_{v\mathbf{k}=\mathbf{K}'}]_z|, \quad (11)$$

yielding a value of $g = 15.06$ identical for both the s - and p -type excitons, and in clear disagreement with experimental results. Another common approximation used in literature, as mentioned above, incorporates the momentum-space profile of the exciton envelope wavefunction (24). Specifically, a weighted average of the single-particle orbital magnetic moment difference over the absolute exciton envelope function squared is calculated to approximate the value for the exciton moment, which makes use of only the first term in our expression in the two-band limit (RHS of Eq. 8):

$$g_n = \frac{1}{\mu_B} \left| \sum_{\mathbf{k} \in \mathbf{K}} |A_{\mathbf{k}}^{n, \mathbf{Q}=0}|^2 [\mu_{c\mathbf{k}} - \mu_{v\mathbf{k}}]_z - \sum_{\mathbf{k}' \in \mathbf{K}'} |A_{\mathbf{k}'}^{n, \mathbf{Q}=0}|^2 [\mu_{c\mathbf{k}'} - \mu_{v\mathbf{k}'}]_z \right|. \quad (12)$$

Here the summation over \mathbf{k} (\mathbf{k}') goes over the points near the \mathbf{K} (\mathbf{K}') valley. The resulting valley g -factors from Eq. 12 for the s - and p -excitons calculated at $\mathbf{Q} = 0$ are presented in Table 1. The s -exciton, whose envelope function is node-less and broadly distributed in \mathbf{k} -space, yields a larger g -factor of 18.45 in this approximation. In contrast, the p -exciton's nodal structure suppresses contributions from the regions of maximal $[\mu_{c\mathbf{k}} - \mu_{v\mathbf{k}}]_z$ (Fig. 2c), reducing its g -factor to 13.03.

To obtain the full quantum result, we employ our main expression given by Eq. 6 for the exciton magnetic moment and compute for the n th exciton level in BBG (which is composed of two valley-degenerate exciton states n_1 and n_2 at $\mathbf{Q} = 0$) the valley g -factor:

$$g_n = \frac{1}{\mu_B} |[\mu_{n_2, \mathbf{Q}=0}^x - \mu_{n_1, \mathbf{Q}=0}^x]_z|, \quad (13)$$

where $\mu_{n_1, \mathbf{Q}=0}^X$ and $\mu_{n_2, \mathbf{Q}=0}^X$ are the exciton orbital magnetic moment of the two valley-related exciton band states (as shown in Fig. 4a), evaluated at COM momentum $\mathbf{Q} = 0$. Using this approach, we obtain $g_s = 20.32$ and $g_p = 1.79$ for the magnetic field induced splitting of the lowest two peaks in the optical spectrum (Fig. 3a) (i.e., the valley g -factor of the lowest s and p exciton states in BBG), respectively. These results are in excellent agreement with experiment and significantly improved over those from previous approximations. Importantly, the theory provides a conceptual understanding why the p -excitons in this system have such anomalously small g factor, highlighting the importance of the new quantum effects captured in our formalism. To further elucidate this, we present the individual contributions to the exciton orbital magnetic moments. Their values for $\mu_{s_1, \mathbf{Q}=0}^X$ and $\mu_{p_1, \mathbf{Q}=0}^X$ are given in Table 2.

We first emphasize that the Berry-phase correction to the single-particle magnetic moment (row 2 in Table 2) is substantial, contributing +2.23 and +3.32 to the g -factor of s - and p -exciton, respectively. This correction, arising even at the single-particle level, has been largely overlooked in the literature, underscoring the importance of accurately evaluating the magnetic moment matrix elements in the Bloch basis. Notably, the enhanced magnitude of this term in the p -exciton is due to the peaked structure of its envelope function in momentum regions where the Berry curvature is the largest (see Fig. S1), thereby amplifying the Berry phase correction term in the \mathbf{k} -space envelope-function summation.

For the relative-motion contribution (row 3 in Table 2), in contrast, it is negligible for the s -exciton (-0.08). This is consistent with its nearly uniform phase in the envelope function, which thus yields a vanishing $\nabla_{\mathbf{k}} A_{\mathbf{k}}^{n\mathbf{Q}}$ and zero phase winding. For the p -exciton, however, we find the envelope function phase winding contribution to the g -factor to be both large and negative (-5.95). Remarkably, this term nearly cancels the positive single-particle moment difference, a cancellation rooted in it's being optical bright with the CWL 2D exciton optical selection rules (37): the phase winding number of the \mathbf{k} -space exciton envelope function is necessarily negative of that of the inter-band optical matrix element $p_{\mathbf{k}\pm} = e_{\pm} \cdot \langle \mathbf{c} \mathbf{k} | \hat{\mathbf{p}} | \mathbf{v} \mathbf{k} \rangle$ in order for the exciton to be optically active, with the latter governed by the pseudospin difference between the conduction and valence bands in BBG (37).

Finally, the COM contribution (row 4 in Table 2) follows a similar trend as the relative motion contribution. The smaller value for the s -exciton (-1.22) compared to the p -exciton (-4.78) reflects its weaker inter- and intra-valley exchange interaction, which results in a less prominent non-analyticity in the exciton band dispersion near $\mathbf{Q} = 0$ as shown in Fig. 4a. In contrast, the stronger exchange interaction in the p -exciton yields a larger magnitude for the COM pseudospin. Notably, the direction of this COM pseudospin is same as envelope function pseudospin because the inter-valley exchange matrix element governing it depends on the transition dipole moment of the exciton state $\langle 0 | \hat{\mathbf{p}} | X_{n0} \rangle$ as described by the effective $\mathbf{Q} \cdot \mathbf{p}$ model (41), which has the same direction of winding as the exciton envelope function. Combined, the relative-motion and COM-motion contributions become comparable to the single-particle contributions but with an opposite sign and strongly suppress the effective g -factor of the p -exciton, in stark contrast to that of the s -exciton, providing a very small valley g -factor in agreement with photocurrent spectroscopy measurements (20). This interplay reveals the crucial roles played by single-particle/exciton band quantum geometry and the character of the exciton envelope-function in shaping the exciton's magnetic response, effects that have not been accounted for in prior theoretical treatments.

Conclusion and outlook

We have derived, within the BSE formalism, a full quantum mechanical expression for the exciton orbital magnetic moment with explicit novel terms of new physical content. Our treatment rigorously accounts for the apparent divergences that arise from the extended nature of the constituent electron and hole band states as well as the extended nature of exciton band states in their COM coordinates. This formulation enables a

comprehensive understanding of how an exciton responds to an external magnetic field, incorporating not only the difference in single-particle magnetic moments of the valence and conduction band states, but also novel contributions associated with the pseudospins and topological effects arising from the relative and COM motion of the e-h pair. Our formalism is general and applicable to systems of any dimensionality under arbitrary magnetic field orientations. As a first application, we have performed ab initio study, based on ab initio GW and GW-BSE calculations, of the orbital magnetic moment and valley g-factor of excitons in BBG, and demonstrated the significance and the accuracy of our approach in capturing experimentally measured exciton valley g-factors and their conceptual understanding. Our results highlight the distinct roles played by single-particle/exciton band Berry connection, e-h relative motion, and exciton COM pseudospins in determining the magnetic response of excitons of different characters. Generalizing our formalism to include second-order perturbation terms will allow us to investigate exciton diamagnetic response and other second-order effects. We anticipate that this framework will serve as a foundational theoretical tool for the study of exciton magnetic behaviors and topology in a wide range of materials, including multi-layer systems (45), moiré heterostructures (46), and topological flat band materials (47), with applications in quantum technologies and information science.

References

1. J. A. Sobota, Y. He, Z.-X. Shen, Angle-resolved photoemission studies of quantum materials. *Reviews of Modern Physics* **93**, (2021).
2. S. W. Koch, M. Kira, G. Khitrova, H. M. Gibbs, Semiconductor excitons in new light. *Nature Materials* **5**, 523–531 (2006).
3. F. J. García de Abajo, Optical excitations in electron microscopy. *Reviews of Modern Physics* **82**, 209–275 (2010).
4. N. P. Wilson *et al.*, Interlayer electronic coupling on demand in a 2D magnetic semiconductor. *Nature Materials* **20**, 1657–1662 (2021).
5. K. L. Seyler *et al.*, Ligand-field helical luminescence in a 2D ferromagnetic insulator. *Nature Physics* **14**, 277–281 (2017).
6. M. Wu, Z. Li, T. Cao, S. G. Louie, Physical origin of giant excitonic and magneto-optical responses in two-dimensional ferromagnetic insulators. *Nature Communications* **10**, (2019).
7. J. R. Schaibley *et al.*, Valleytronics in 2D materials. *Nature Reviews Materials* **1**, (2016).
8. J. Yin *et al.*, Tunable and giant valley-selective Hall effect in gapped bilayer graphene. *Science* **375**, 1398–1402 (2022).
9. S. L. Bayliss *et al.*, Optically addressable molecular spins for quantum information processing. *Science* **370**, 1309–1312 (2020).
10. M. Liebich *et al.*, Controlling Coulomb correlations and fine structure of quasi-one-dimensional excitons by magnetic order. *Nature Materials* **24**, 384–390 (2025).
11. M. R. Wasielewski *et al.*, Exploiting chemistry and molecular systems for quantum information science. *Nature Reviews Chemistry* **4**, 490–504 (2020).

12. D. Y. Qiu, F. H. da Jornada, S. G. Louie, Optical Spectrum of MoS₂: Many-Body Effects and Diversity of Exciton States. *Physical Review Letters* **111**, (2013).
13. K. F. Mak, D. Xiao, J. Shan, Light–valley interactions in 2D semiconductors. *Nature Photonics* **12**, 451–460 (2018).
14. D. Xiao, W. Yao, Q. Niu, Valley-Contrasting Physics in Graphene: Magnetic Moment and Topological Transport. *Physical Review Letters* **99**, (2007).
15. R. Schmidt *et al.*, Magnetic-Field-Induced Rotation of Polarized Light Emission from Monolayer WS₂. *Physical Review Letters* **117**, (2016).
16. D. MacNeill *et al.*, Breaking of Valley Degeneracy by Magnetic Field in Monolayer MoSe₂. *Physical Review Letters* **114**, (2015).
17. G. Aivazian *et al.*, Magnetic control of valley pseudospin in monolayer WSe₂. *Nature Physics* **11**, 148–152 (2015).
18. A. V. Stier *et al.*, Magneto-optics of Exciton Rydberg States in a Monolayer Semiconductor. *Physical Review Letters* **120**, (2018).
19. A. Srivastava *et al.*, Valley Zeeman effect in elementary optical excitations of monolayer WSe₂. *Nature Physics* **11**, 141–147 (2015).
20. L. Ju *et al.*, Tunable excitons in bilayer graphene. *Science* **358**, 907–910 (2017).
21. T. Woźniak, P. E. Faria Junior, G. Seifert, A. Chaves, J. Kunstmann, Exciton g-factors of van der Waals heterostructures from first-principles calculations. *Physical Review B* **101**, (2020).
22. F. Xuan, S. Y. Quek, Valley Zeeman effect and Landau levels in two-dimensional transition metal dichalcogenides. *Physical Review Research* **2**, (2020).
23. J. Förste *et al.*, Exciton g-factors in monolayer and bilayer WSe₂ from experiment and theory. *Nature Communications* **11**, (2020).
24. T. Deilmann, P. Krüger, M. Rohlfing, Ab Initio Studies of Exciton g-factors: Monolayer Transition Metal Dichalcogenides in Magnetic Fields. *Physical Review Letters* **124**, (2020).
25. E. I. Blount, Formalisms of Band Theory. *Solid State Physics*, 305–373 (1962).
26. R. Resta, Electrical polarization and orbital magnetization: the modern theories. *Journal of Physics: Condensed Matter* **22**, (2010).
27. J. Shi, G. Vignale, D. Xiao, Q. Niu, Quantum Theory of Orbital Magnetization and Its Generalization to Interacting Systems. *Physical Review Letters* **99**, (2007).
28. P. E. Faria Junior, D. Hernangómez-Pérez, T. Amit, J. Fabian, S. Refaely-Abramson, Generalized many-body exciton g-factors: magnetic hybridization and non-monotonic Rydberg series in monolayer WSe₂. 2025 (10.48550/arXiv.2505.18468).
29. M. S. Hybertsen, S. G. Louie, Electron correlation in semiconductors and insulators: Band gaps and quasiparticle energies. *Physical Review B* **34**, 5390–5413 (1986).

30. M. Rohlfing, S. G. Louie, Electron-hole excitations and optical spectra from first principles. *Physical Review B* **62**, 4927–4944 (2000).
31. F. Mauri, S. G. Louie, Magnetic Susceptibility of Insulators from First Principles. *Physical Review Letters* **76**, 4246–4249 (1996).
32. G. Vignale, Orbital paramagnetism of electrons in a two-dimensional lattice. *Physical Review Letters* **67**, 358–361 (1991).
33. M.-C. Chang, Q. Niu, Berry phase, hyperorbits, and the Hofstadter spectrum: Semiclassical dynamics in magnetic Bloch bands. *Physical Review B* **53**, 7010–7023 (1996).
34. W. Yao, Q. Niu, Berry Phase Effect on the Exciton Transport and on the Exciton Bose-Einstein Condensate. *Physical Review Letters* **101**, (2008).
35. D. Xiao, J. Shi, Q. Niu, Berry Phase Correction to Electron Density of States in Solids. *Physical Review Letters* **95**, (2005).
36. D. Xiao, M.-C. Chang, Q. Niu, Berry phase effects on electronic properties. *Reviews of Modern Physics* **82**, 1959–2007 (2010).
37. T. Cao, M. Wu, S. G. Louie, Unifying Optical Selection Rules for Excitons in Two Dimensions: Band Topology and Winding Numbers. *Physical Review Letters* **120**, (2018).
38. E. V. Castro *et al.*, Biased Bilayer Graphene: Semiconductor with a Gap Tunable by the Electric Field Effect. *Physical Review Letters* **99**, (2007).
39. Y. Zhang *et al.*, Direct observation of a widely tunable bandgap in bilayer graphene. *Nature* **459**, 820–823 (2009).
40. C.-H. Park, N. Marzari, Berry phase and pseudospin winding number in bilayer graphene. *Physical Review B* **84**, (2011).
41. D. Y. Qiu, T. Cao, S. G. Louie, Nonanalyticity, Valley Quantum Phases, and Lightlike Exciton Dispersion in Monolayer Transition Metal Dichalcogenides: Theory and First-Principles Calculations. *Physical Review Letters* **115**, (2015).
42. F. Wu, F. Qu, A. H. MacDonald, Exciton band structure of monolayer MoS₂. *Physical Review B* **91**, (2015).
43. L. Y. Liu *et al.*, Direct Observation of Massless Excitons and Linear Exciton Dispersion. 2025 (10.48550/arXiv.2502.20454).
44. D. Y. Qiu, G. Cohen, D. Novichkova, S. Refaely-Abramson, Signatures of Dimensionality and Symmetry in Exciton Band Structure: Consequences for Exciton Dynamics and Transport. *Nano Letters* **21**, 7644–7650 (2021).
45. J. Yang *et al.*, Spectroscopy signatures of electron correlations in a trilayer graphene/hBN moiré superlattice. *Science* **375**, 1295–1299 (2022).
46. M. H. Naik *et al.*, Intralayer charge-transfer moiré excitons in van der Waals superlattices. *Nature* **609**, 52–57 (2022).

47. G. Sethi, Y. Zhou, L. Zhu, L. Yang, F. Liu, Flat-Band-Enabled Triplet Excitonic Insulator in a Diatomic Kagome Lattice. *Physical Review Letters* **126**, (2021).
48. P. Giannozzi *et al.*, QUANTUM ESPRESSO: a modular and open-source software project for quantum simulations of materials. *Journal of Physics: Condensed Matter* **21**, (2009).
49. D. R. Hamann, Optimized norm-conserving Vanderbilt pseudopotentials. *Physical Review B* **88**, (2013).
50. T. Sohler, M. Calandra, F. Mauri, Density functional perturbation theory for gated two-dimensional heterostructures: Theoretical developments and application to flexural phonons in graphene. *Physical Review B* **96**, (2017).
51. G. Giovannetti, P. A. Khomyakov, G. Brocks, P. J. Kelly, J. van den Brink, Substrate-induced band gap in graphene on hexagonal boron nitride: Ab initio density functional calculations. *Physical Review B* **76**, (2007).
52. J. Deslippe *et al.*, BerkeleyGW: A massively parallel computer package for the calculation of the quasiparticle and optical properties of materials and nanostructures. *Computer Physics Communications* **183**, 1269–1289 (2012).
53. F. H. da Jornada, D. Y. Qiu, S. G. Louie, Nonuniform sampling schemes of the Brillouin zone for many-electron perturbation-theory calculations in reduced dimensionality. *Physical Review B* **95**, (2017).
54. G. Pizzi *et al.*, Wannier90 as a community code: new features and applications. *Journal of Physics: Condensed Matter* **32**, (2020).
55. D. Culcer, Y. Yao, Q. Niu, Coherent wave-packet evolution in coupled bands. *Physical Review B* **72**, (2005).
56. Y. H. Kwan, Y. Hu, S. H. Simon, S. A. Parameswaran, Exciton Band Topology in Spontaneous Quantum Anomalous Hall Insulators: Applications to Twisted Bilayer Graphene. *Physical Review Letters* **126**, (2021).
57. P. Li, I. Appelbaum, Excitons without effective mass: Biased bilayer graphene. *Physical Review B* **99**, (2019).

Acknowledgements: We thank Xiaoxun Gong, Jack McArthur, and Shang Ren for the fruitful discussions.

Funding: This work was primarily supported by the Center for Computational Study of Excited-State Phenomena in Energy Materials (C2SEPEM) at LBNL, funded by the U.S. Department of Energy, Office of Science, Basic Energy Sciences, Materials Sciences and Engineering Division under Contract No. DE-AC02-05CH11231, as part of the Computational Materials Sciences Program which provided the developments of the theory, advanced codes and simulations, as well as the *GW* and *GW*-BSE calculations of e-h interactions and exciton properties. Additional support was provided by the National Science Foundation under Grant No. DMR-2325410, which provided topological and gauge invariance analyses and ab initio calculations of exciton magnetic moments. Computational resources were provided by National Energy Research Scientific Computing Center (NERSC), supported by the Office of Science of the U.S. Department of Energy under Contract No. DE-AC02-05CH11231; Stampede2 at the Texas Advanced Computing Center (TACC), the University of Texas at Austin, through Extreme Science and Engineering Discovery Environment (XSEDE),

supported by the National Science Foundation under Grant No. ACI-1053575; and Frontera at TACC, supported by the National Science Foundation under Grant No. OAC-1818253.

Author contributions: S.G.L. conceived the research direction and, together with G.S., proposed the project. G.S. developed the quantum theory of the exciton magnetic moment, performed all numerical simulations, and wrote the initial draft of the manuscript. J.R. contributed to the derivation of perturbed exciton Hamiltonian including the treatment of position operator in Bloch basis. F.Z., and C.H. helped with the ab initio calculations of biased bilayer graphene. W.T. contributed to the development of the exciton wave-packet formalism. M.N. assisted with the magnetic moment calculations. S.G.L. supervised the project, guided the theoretical analysis, and interpreted the results. All authors discussed the findings and contributed to revising the final manuscript.

Competing interests: The authors declare no competing interests.

Data availability: All data supporting this study are provided in the main text or supplementary materials (SM). The calculations presented in the paper were carried out using publicly available electronic structure codes as described in SM. Our findings can be fully reproduced using these codes and following the procedure outlined in the paper.

Supplementary Materials:

Methods

Supplementary text

Figs S1 to S4

References (48-57)

Figures

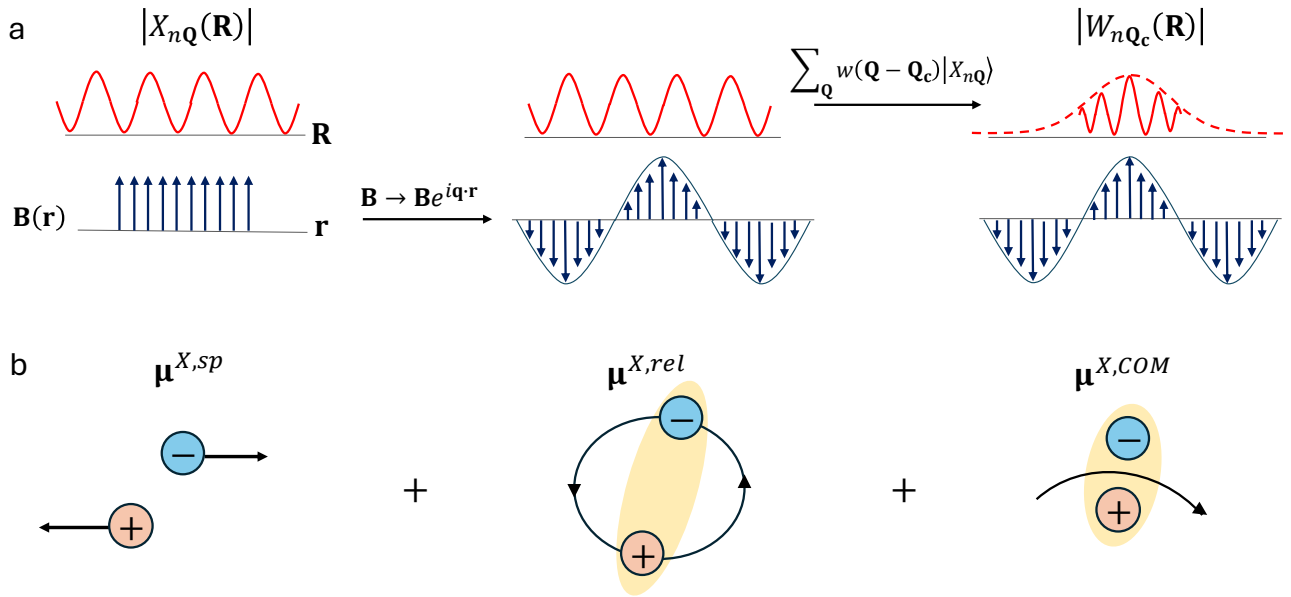


Fig. 1: Schematic overview of quantum formalism for exciton magnetic moment. **a**, A conceptual framework for deriving the quantum many-body response of an exciton state $|X_{nQ}\rangle$, which is a Bloch state extending over the crystal, to an external uniform magnetic field $\mathbf{B}(\mathbf{r})$. *Left*: Schematic of an exciton state in a uniform \mathbf{B} field. Two mathematical divergences arise due to the long-range nature of the position operator in the Bloch basis - one associated with the single-particle wavefunction (in \mathbf{k} or \mathbf{r}) and the other with the exciton

COM Bloch wavefunction (in \mathbf{Q} or \mathbf{R}). *Middle*: To resolve the \mathbf{k} -space divergence, the position operator is replaced with its periodic analog. This procedure is equivalent to simulating the response to a periodic magnetic field and yields well-defined single-particle matrix elements, but the divergence associated with \mathbf{Q} remains. *Right*: A localized excitonic wave-packet is constructed in \mathbf{R} , $|W_{n\mathbf{Q}_c}\rangle = \sum_{\mathbf{Q}} w(\mathbf{Q} - \mathbf{Q}_c) |X_{n\mathbf{Q}}\rangle$, to regularize the divergence arising from the extended COM Bloch states. After obtaining a well-defined expression, the long-wavelength limit of the magnetic field is taken, followed by delocalization of the wave-packet. The order of limits is essential. **b**, Final expression for the exciton magnetic moment is composed of three physically distinct contributions: (1) $\mu_{n\mathbf{Q}}^{X,sp}$ related to the difference between the single-particle Berry-phase corrected magnetic moments of the individual electron and hole, (2) $\mu_{n\mathbf{Q}}^{X,rel}$ related to the envelope function phase winding in \mathbf{k} -space from relative e-h motions, and (3) $\mu_{n\mathbf{Q}}^{X,COM}$ the COM contribution in \mathbf{Q} -space linked to quantum geometry of exciton band and pseudospin texture.

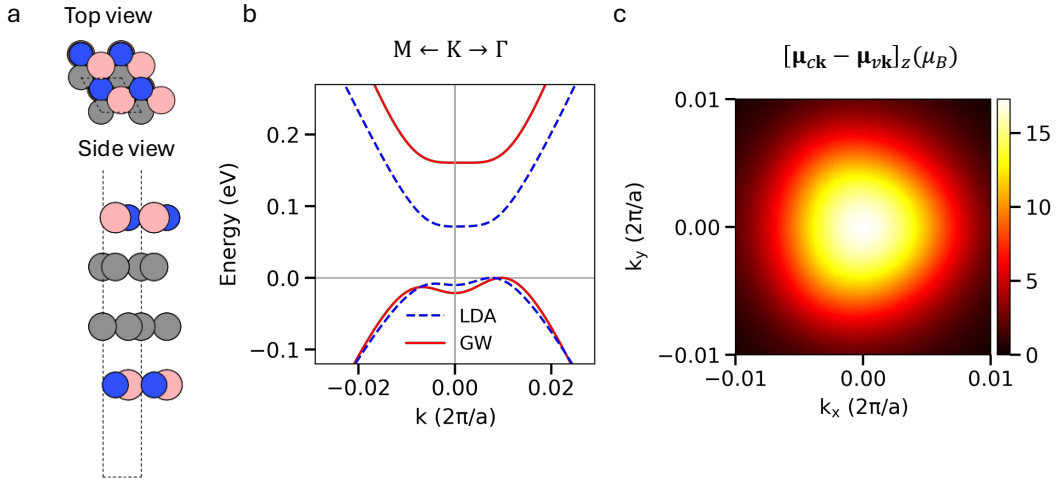


Fig. 2: Quasiparticle band structure and single-particle magnetic moment of BBG. **a**, Atomic configuration of BBG with hBN monolayer on both sides used to simulate the effect of hBN encapsulation in experiment. Top-view (top panel) and side-view (bottom panel) of the structure are shown. Grey color balls denote carbon atoms, while blue and pink balls denote nitrogen and boron atoms respectively. Dashed lines indicate the boundaries of the unit-cell. Carbon atoms on sites forming interlayer dimer are indicated as those on the vertical dashed line, while the other carbon atom in each layer is on a non-dimer site. Boron is placed as nearest-neighbor atom next to a carbon on the non-dimer sites of BBG which has the most contribution to the states at the valence and conduction band edges. **b**, Electronic band structure of BBG with hBN encapsulation calculated using DFT-LDA (blue dashed) and using GW (red solid) near the K-valley. The GW self-energy correction significantly enlarges the band gap and alters the dispersion near the K point. **c**, The difference between the orbital magnetic moments (along z direction which is normal to the atomic planes) for the conduction- and valence-band states near the K-point in units of Bohr magneton (μ_B). The plot is centered at the (0,0) point which corresponds to $\mathbf{k} = \mathbf{K}$, where the moment difference peaks, highlighting the valley-localization of the exciton envelope function in BBG. The non-zero value in the difference arises due to particle-hole asymmetry. The result for the \mathbf{K}' -valley is negative of that for the \mathbf{K} -valley owing to time-reversal symmetry. These characteristic features contribute to the single-particle component of the exciton orbital magnetic moment - $\mu_{n\mathbf{Q}}^{X,sp}$.

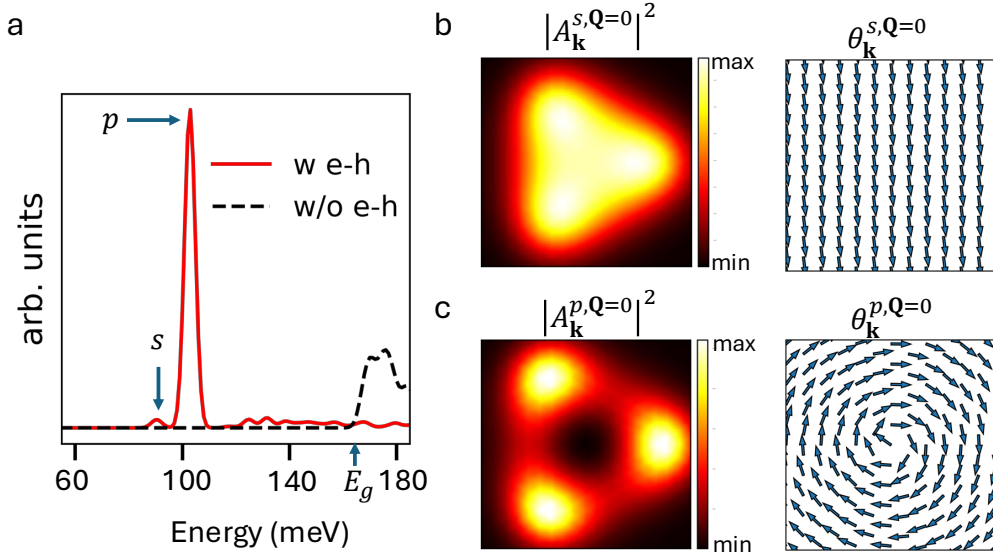


Fig. 3: Optical spectrum and exciton states of BBG at $\mathbf{Q} = 0$. **a**, Optical absorption spectra for linearly polarized light calculated with (red) and without (black) e-h interactions. Excitonic effects give rise to a number of peaks below the band gap. The two lowest peaks correspond to the lowest s - and p -like exciton states that are both two-fold (valley) degenerate. **b** and **c**, Momentum-resolved amplitude square and phase maps near the K-valley of the exciton envelope function for one of the s - and p - excitons, respectively. Axis labels are the same as those used in Fig. 2c, facilitating comparison between envelope function structure and the single-particle orbital magnetic moment landscape in \mathbf{k} -space. The s -exciton displays no nodes or phase winding, while the p -exciton exhibits a single nodal feature at the center of the plot and a phase winding number of +1, consistent with angular momentum $l = 1$. These characteristic features contribute to the e-h relative motion component of the exciton magnetic moment - $\mu_{n\mathbf{Q}}^{x,rel}$.

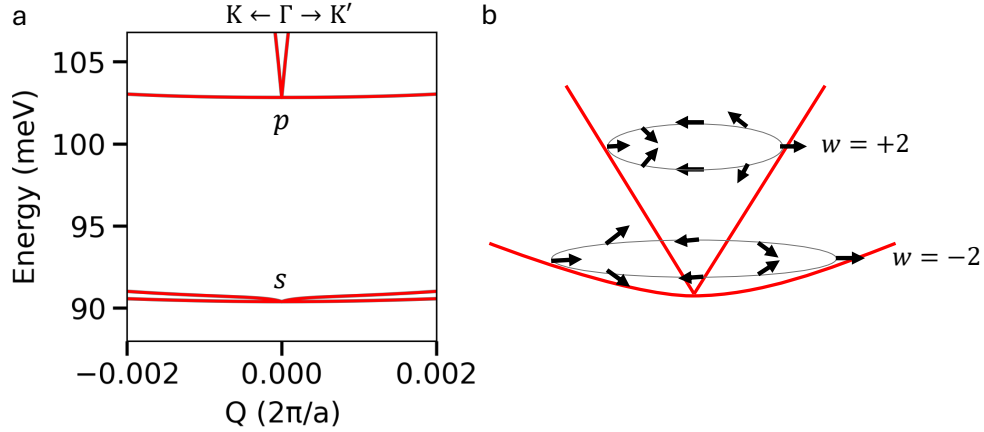


Fig. 4: Exciton band structure and pseudospin texture of BBG in \mathbf{Q} -space. **a**, Exciton dispersion near $\mathbf{Q} = 0$ along K- Γ -K' path in the BZ, showing the valley-degenerate doublet at $\mathbf{Q} = 0$ and its splitting at finite COM momentum due to inter- and intra-valley exchange. The p -exciton exhibits a characteristic nonanalytic v-shaped upper branch and a parabolic lower branch. This effect is less pronounced for the s -exciton. Under a magnetic field the bands at $\mathbf{Q} = 0$ are no longer degenerate. This band splitting under a field characterizes the valley g-factor, described by the difference in magnetic moments of the exciton bands at $\mathbf{Q} = 0$. **b**, Exciton

pseudospin textures associated with the p -exciton branches. The upper, nonanalytic branch carries a phase winding number (associated with the valley pseudospin, i.e. the valley components of the exciton) of +2, and the lower, parabolic branch exhibits a winding of -2 , reflecting the valley-encoded COM angular momentum. These characteristic features contribute to the e-h COM motion component of the exciton magnetic moment - $\mu_{nQ}^{X,COM}$.

Tables

Table 1: Comparison of calculated and experimental exciton g -factors in BBG. Valley exciton g -factors for the s - and p -like excitons obtained using three different levels of theory and compared with experimentally measured values. Calculated results: a) single-particle approximation which neglects e-h interaction and electronic band geometric effects; b) same as (a) but weighted in k -space by the modulus square of the exciton envelope function; c) the full quantum formalism including electron band structure and exciton band structure Berry-phase corrections, exciton envelope function phase winding, and e-h COM motion contributions as given by Eq. 6. Experimental values are extracted from the peak splitting in photocurrent spectroscopy (20). The values presented are $g_n = \frac{1}{\mu_B} \left| [\mu_{n_2,Q=0}^X - \mu_{n_1,Q=0}^X]_z \right|$ with different levels of theory in computing μ^X . For the experimental value of s -exciton, the uncertainty reflects the fitting error in peak splitting. For the p -exciton, no explicit experimental value was reported in ref. (20); based on experimentalists' estimate that the splitting is 20% of the linewidth, the valley g -factor for p -exciton is extracted with uncertainties derived from the linewidth variation across magnetic fields. The g -factors are dimensionless.

	g_s	g_p
a) Free electron-hole pair approximation with no Berry-curvature effect (Eq. 11)	15.06	15.06
b) Exciton envelope function averaged over k -space of values in 1) (Eq. 12)	18.45	13.03
c) Full quantum mechanical treatment (Eq. 6 and Eq. 13)	20.32	1.79
d) Experimental measured values (20)	19.8 ± 0.1	1.4 ± 0.8

Table 2: Decomposition of computed exciton orbital magnetic moment into different physical contributions. Values in the first four rows correspond to the three distinct physical contributions to $\mu_{s_1,Q=0}^X$ and $\mu_{p_1,Q=0}^X$ as defined in Eq. 7. The sum of the first two rows gives the Berry-phase-corrected single-particle contribution from the conduction and valence band states that compose the exciton, i.e., the term $\mu_{nQ}^{X,sp}$. The third and fourth rows give the contributions from the envelope function winding (arising from relative e-h motion, $\mu_{nQ}^{X,rel}$) and from the exciton band quantum geometry ($\mu_{nQ}^{X,COM}$), respectively. The final row shows the total $\mu_{s_1,Q=0}^X$ and $\mu_{p_1,Q=0}^X$ for the s - and p -exciton states of BBG. The values for $\mu_{s_2,Q=0}^X$ and $\mu_{p_2,Q=0}^X$ are negative of those of their counterparts. All values are in the unit of Bohr magneton (μ_B).

	s	p
Envelope function average	9.23	6.52
Berry phase correction to e and h moments	2.23	3.32
e-h relative moment	-0.08	-5.95

e-h COM moment	−1.22	−4.78
Total exciton orbital magnetic moment	10.16	−0.89